Dynamics of stress-induced domain wall motion

M. T. Bryan, J. Dean, and D. A. Allwood
Department of Materials Science and Engineering, University of Sheffield, Sheffield S1 3JD, United Kingdom

(Received 14 February 2012; published 13 April 2012)

Magnetic domain wall motion caused by nonuniform stress in a magnetostrictive nanowire was studied using a semianalytical model. The study reveals that the axial stress gradient is responsible for domain wall motion, even in the absence of an applied magnetic field or spin-polarized current, and agrees well with previous micromagnetic calculations. Walls moving into a stress-induced energy well reach a maximum velocity that depends on the stress gradient, before undergoing damped oscillatory motion. This model will inform the development of emerging artificial multiferroic systems.

DOI: 10.1103/PhysRevB.85.144411 PACS number(s): 75.78.Fg, 75.78.Cd, 77.55.Nv, 85.70.Ec

Switching of magnetic nanowires often occurs via domain wall propagation driven by an axial magnetic field,[1] a spin-polarized current,[2] or a combination of the two.[3,4] The dynamic behavior of domain walls during field- and current-driven motion has been well characterized analytically,[5] micromagnetically,[6] and experimentally.[1–4] Wall motion is sensitive to a wide variety of factors, including the nanowire dimensions,[7,8] anisotropy,[9–11] and transverse components of the magnetic field.[12–16] Recently, studies of multiferroic systems have shown that magnetic domain walls may be moved without an applied magnetic field or current.[17–19] Furthermore, this may achieved with low switching energies,[18] highlighting the potential of multiferroics as low-power memory devices. In intrinsic multiferroics, ferroelectric and magnetic domains coexist in the same material with a collinear arrangement, so electrical manipulation of ferroelectric domains directly causes magnetic domain wall propagation.[19] However, in artificial multiferroics, where ferroelectric and magnetic properties occur in neighboring materials, electrical control over magnetic domain wall motion must be driven by a different mechanism. For example, stress generated by a piezoelectric material may induce anisotropy in the magnetostrictive layer of an artificial multiferroic to generate wall motion.[18] Uniform anisotropy is predicted[9,11] and demonstrated[10] to modify wall dynamics, but cannot induce wall motion in the absence of a driving field or current. Nonuniform stress-induced anisotropy must be considered to understand the mechanism behind the stress-induced wall motion. In this paper, we derive general one-dimensional (1D) equations of motion for domain walls moving through regions of nonuniform stress and compare the solutions with the wall dynamics predicted by micromagnetic modeling. The semianalytical solutions provide a clear physical description of the system without the computational effort required for micromagnetic models.

Before deriving the equations of motion, we first consider the generation of a suitable stress profile for comparison with the micromagnetic model. We use a 5-nm-thick, 100-nm-wide magnetostrictive nanowire, sandwiched between a Si substrate and a 200-nm-thick piezoelectric layer, shown in Fig. 1, and assume perfect coupling of stress between the layers. Above the piezoelectric are three 100-nm-wide contacts with center-to-center separation s. The central contact (contact 2, Fig. 1) is held at potential V_C, while the outer contacts are held at ground. To isolate the contribution of the stress-induced anisotropy, and for comparison with previous work,[18] we model the nanowire with magnetic properties similar to those of Permalloy (magnetocrystalline anisotropy $K = 0$ J m^{-3}, exchange constant $A = 10$ pJ m^{-1}, saturation magnetization $M_S = 800$ kA m^{-1}, and Gilbert damping constant $\alpha = 0.02$), but with magnetoelastic properties similar to those of bulk $Fe_{83}Ga_{17}$ (Young's modulus $Y_{FeGa} = 100$ GPa, Poisson's ratio $\nu_{FeGa} = 0.3$, magnetostriction constants $\lambda_s = \lambda_{100} = \lambda_{111} = 200$ ppm).[20,21] The piezoelectric layer is poled along the wire length (the x axis) and has the properties of lead zirconate titanate:[22] Young's modulus $Y_{PZT} = 100$ GPa, Poisson's ratio $\nu_{PZT} = 0.3$, transverse strain constant $d_{13} = -265 \times 10^{-12}$ m V^{-1}, and extensional strain constant $d_{33} = 585 \times 10^{-12}$ m V^{-1}. The stress tensor generated at every point in the nanowire due to V_C is calculated using the finite-element package COMSOL.[23,24] The stress tensor is composed of six independent components σ_{ij}, where $i,j = x,y,z$ (coordinate axes defined in Fig. 1). Components with $i = j$ describe the normal stresses acting along the nanowire axes, while shear stresses are described when $i \neq j$. Averaging each stress component across the wire width and thickness enables the generation of 1D stress profiles.

Figures 2(a)–2(f) summarize the change in stress with the potential V_C applied to the central contact for a fixed contact spacing of $s = 300$ nm. Each stress component has a unique spatial profile, with the relative strengths of the different components being strongly position dependent. Indeed, although the σ_{xx} component dominates in general [Fig. 2(a)], the σ_{xz} component [Fig. 2(c)] dominates in the region directly below the central contact. The σ_{zz}, σ_{xy}, and σ_{yz} components [Figs. 2(d)–2(f)] are negligible across the wire length. Modifications of V_C generate proportional changes in the magnitude of each stress component, but the general form of each profile remains unchanged, reflecting the linear response of the piezoelectric layer to an applied electric field. On the other hand, increasing s results in stress profiles that are broader but have lower amplitude (Fig. 3). In every case, σ_{xx} dominates the energy landscape [Fig. 2(g)], such that the lowest-energy magnetic domain wall position is coincident with the minimum in σ_{xx}. For simplicity, we have considered only the response of the piezoelectric lattice to V_C and have neglected "extrinsic" stress contributions from defects and ferroelectric domain walls, although in a real system these contributions can be significant.[25] Stress from ferroelectric

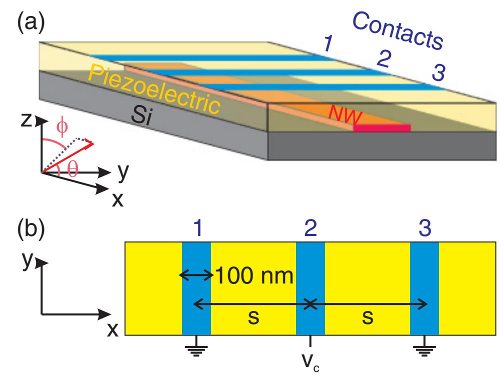

FIG. 1. (Color online) (a) Schematic diagram of the nanowire (NW) sandwiched between a Si substrate and a piezoelectric layer topped with three electrical contacts. (b) Top view of the schematic, showing the potential configuration and contact spacing.

domain walls may be expected to superimpose additional localized energy minima in the energy landscape, coupling ferroelectric and magnetic domain walls and providing a mechanism for the observed ferroelectric wall-like reversible motion of electrically controlled magnetic domain walls in artificial multiferroics.[17]

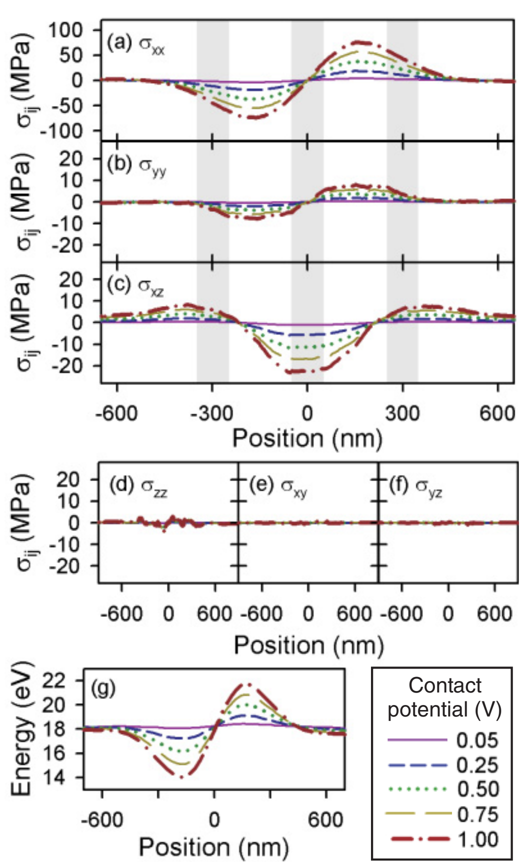

FIG. 2. (Color online) Effect of the potential on the central contact, V_C, on the 1D profile of each stress component σ_{ij}, for $ij =$ (a) xx, (b) yy, (c) xz, (d) zz, (e) xy, and (f) yz. The shaded regions in (a)–(c) indicate the positions of the three contacts ($s = 300$ nm). (g) The effect of the wall position on the total energy, calculating the stress-induced anisotropy energy using the full 3D stress map.

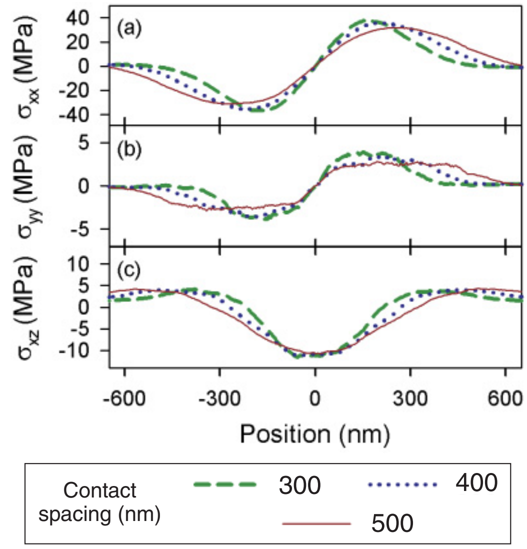

FIG. 3. (Color online) The effect of the contact spacing s on the stress profiles of (a) σ_{xx}, (b) σ_{yy}, and (c) σ_{xz} at $V_C = 0.5$ V.

We now derive a 1D semianalytical model to help identify the origin of stress-induced motion and then apply the stress profiles calculated in Fig. 2 to compare the results with the equivalent micromagnetic case.[18] The structure of a domain wall in a nanowire is defined by $\sin\theta = (\cosh u)^{-1}$, $\cos\theta = -\tanh u$, $u = (x - q)/\Delta$, and $d\theta/dx = \sin\theta/\Delta$, where θ is the polar magnetization angle (Fig. 1), q is the x position of the domain wall center, and Δ is the wall width parameter.[5] We define the width of the domain wall as $\pi\Delta$ such that at the edge of the wall $x = q \pm \pi\Delta/2$ and $\theta \approx 0$ or π. Following Slonczewski,[26] we solve the Landau-Lifshitz-Gilbert equation for a domain wall under the influence of an axial field H_x, but include an additional generalized term to describe a spatially varying energy density (see Appendix A for details):

$$\dot{\varphi} = \frac{1}{2(1+\alpha^2)}[2\gamma_0 H_x + \alpha\gamma_0 M_S(N_z - N_y)\sin 2\varphi + \alpha f + g], \tag{1}$$

$$\dot{q} = \frac{\Delta}{2\alpha}[2\gamma_0 H_x + g - 2\dot{\varphi}], \tag{2}$$

$$f = \int_{q-\pi\Delta/2}^{q+\pi\Delta/2} \frac{-\gamma_0}{\mu_0 M_S}\frac{\delta W_k}{\delta\varphi}\frac{1}{\Delta}dx, \tag{3}$$

$$g = \int_{q-\pi\Delta/2}^{q+\pi\Delta/2} \frac{\gamma_0}{\mu_0 M_S}\frac{\delta W_k}{\delta\theta}\frac{\sin\theta}{\Delta}dx, \tag{4}$$

where φ is the azimuthal angle of the magnetization in the domain wall (Fig. 1), γ_0 is the gyromagnetic ratio, μ_0 is the permeability of free space, N_y and N_z are demagnetization factors in the y and z directions, δ indicates a functional derivative, $\dot{q}$ is the wall velocity, and $\dot{\varphi}$ is the azimuthal angular velocity. Although we shall use W_k to describe the stress-induced energy density, the equations are general, so Eqs. (3) and (4) could describe any energy term in addition to the Zeeman and demagnetization energies. In particular, the model described here may be readily adapted to describe any spatially varying anisotropy. Equations (3) and (4) are integrated over the width of the domain wall, so spatial variations of W_k beyond the wall boundaries have no effect on the wall behavior.

In order to achieve a generalized solution for any stress distribution, we make an assumption that on the length scale of the wall width each stress component σ_{ij} depends linearly on the distance from the wall center. For any position x along the wire, this gives $\sigma_{ij} = \tilde{\sigma}_{ij} + \tilde{\sigma}'_{ij}(x - q)$, where $\tilde{\sigma}_{ij}$ is the ij stress component at the center of the domain wall and $\tilde{\sigma}'_{ij}$ is the corresponding stress gradient. When integrating this numerically, the values of $\tilde{\sigma}_{ij}$ and $\tilde{\sigma}'_{ij}$ are recalculated after each time step from known stress profiles (e.g., Fig. 2), allowing the stress and gradient to evolve as the wall position changes. Provided the stress changes are small over the length scale of the wall width, this locally linear approximation provides a reasonable first-order approximation of the effect of nonuniform stress on a domain wall at any given position, while allowing arbitrary stress profiles to be described.

The stress-induced energy density in a cubic magnetostrictive system is given by

$$W_k = -\tfrac{3}{2}\lambda_s\big(\sigma_{xx}\alpha_x^2 + \sigma_{yy}\alpha_y^2 + \sigma_{zz}\alpha_z^2 + 2\sigma_{xy}\alpha_x\alpha_y + 2\sigma_{yz}\alpha_y\alpha_z + 2\sigma_{xz}\alpha_x\alpha_z\big), \tag{5}$$

where $\alpha_x = \cos\theta, \alpha_y = \sin\theta\sin\varphi$, and $\alpha_z = \sin\theta\cos\varphi$. Substituting Eq. (5) into Eqs. (3) and (4) and integrating by parts (see Appendix B for details), we obtain

$$f = \frac{3\gamma_0\lambda_s}{\mu_0 M_S}[\pi\Delta(\tilde{\sigma}'_{xz}\sin\varphi - \tilde{\sigma}'_{xy}\cos\varphi) + (\tilde{\sigma}_{yy} - \tilde{\sigma}_{zz})\sin 2\varphi + 2\tilde{\sigma}_{yz}\cos 2\varphi], \tag{6}$$

$$g = \frac{-3\gamma_0\lambda_s}{2\mu_0 M_S}\pi\Delta\tilde{\sigma}'_{xx}, \tag{7}$$

which are substituted into Eqs. (1) and (2) to describe the equations of the wall motion. The domain wall width parameter, derived in Appendix C, is given by

$$\Delta = \sqrt{\frac{A}{\frac{1}{2}\mu_0 M_S^2(N_y\sin^2\varphi + N_z\cos^2\varphi) - \frac{3}{2}\lambda_s(\tilde{\sigma}_{yy}\sin^2\varphi + \tilde{\sigma}_{zz}\cos^2\varphi + \tilde{\sigma}_{yz}\sin 2\varphi)}}. \tag{8}$$

The stress components at the center of the wall ($\tilde{\sigma}_{yy}, \tilde{\sigma}_{zz}$, and $\tilde{\sigma}_{yz}$) introduce anisotropy terms into the equations of motion, as in the case of uniform stress.[11] On the other hand, the stress gradients $\tilde{\sigma}'_{xx}$, $\tilde{\sigma}'_{xy}$, and $\tilde{\sigma}'_{xz}$ result in terms that affect the wall velocity and azimuthal angle in a similar fashion to applied fields (H_x, H_y, and H_z, respectively). There are, however, important differences between the stress gradient terms and true fields: the stress gradients do not affect the wall width or cause domain canting,[12] so the magnetization always rotates by 180° across the wall.

If $\dot{\varphi} = 0$, the stress-induced wall velocity, found from Eq. (2) when $H_x = 0$, becomes constant at $\dot{q} = \Delta g/2\alpha$. Using Eq. (1), the Walker breakdown field can be generalized to $H_w + 0.5g_w = -0.5\alpha M_S(N_z - N_y)\sin 2\varphi_w - 0.5\alpha f_w/\gamma_0$, where the w subscripts indicate that the quantities are evaluated at the cusp of Walker breakdown, when $d\dot{\varphi}/d\varphi = \dot{\varphi} = 0$. However, as f and g may change with wall position, the conditions for these extreme cases may not necessarily be satisfied for a significant period of the wall motion. Therefore wall behavior under specific stress profiles must be considered.

Using the stress profiles when $V_C = 0.5$ V and $s = 300$ nm (Fig. 2), a semianalytical solution (SA1) to the equations of motion can be found. Figure 4 shows a comparison between the previous micromagnetically calculated wall velocity profile[18] and the velocities found using SA1 and a modified version of the semianalytical model SA2 (described below). All plots show damped oscillations in the wall velocity as the wall moves around the energy minimum [Fig. 4(a)]. The oscillations are not due to Walker breakdown, but instead are due to opposite $\tilde{\sigma}'_{xx}$ occurring on either side of the energy minimum.

Close to the energy minimum the spatial dependence of the wall velocity predicted by SA1 matches with the micromagnetic model [Fig. 4(b)]. However, the peak velocity predicted by SA1 is much smaller and the period of the oscillations much longer than occurs in the micromagnetic model. One reason for this discrepancy is that 1D models tend to underpredict the wall velocity,[8] as the analytical wall width

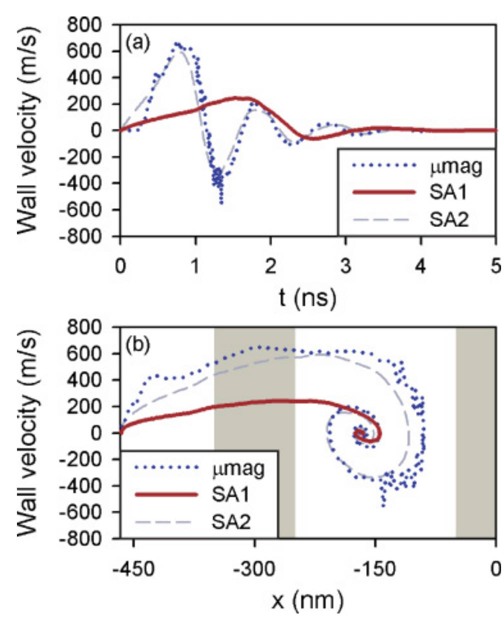

FIG. 4. (Color online) (a) Temporal and (b) spatial evolution of the wall velocity calculated using the micromagnetic (μmag) and semianalytical (SA1 and SA2) models when $s = 300$ nm and $V_C = 0.5$ V. The shaded regions in (b) show the positions of the electrical contacts.

parameter is usually smaller than the average micromagnetic equivalent. In this system, where the spatial position feeds back to the factors affecting the wall dynamics, the underprediction of wall velocity leads to large differences between the wall oscillations predicted by the two models. Comparison between the micromagnetic and analytical wall profiles in the absence of stress suggests that the micromagnetic wall width parameter is a factor of 1.78 larger than suggested by Eq. (8). If this scaling factor to Δ is included in the semianalytical model (SA2), there is excellent agreement between the wall oscillations of the micromagnetic and semianalytical models (Fig. 4). In addition, the magnetic fields needed to depin the wall past the energy maximum, 3.1 $\mathrm{kA\,m^{-1}}$ in SA1 and 4.8 $\mathrm{kA\,m^{-1}}$ in SA2 (not shown), are close to the 3.2 $\mathrm{kA\,m^{-1}}$ calculated micromagnetically.[18] This suggests that the simplifications made in the semianalytical model capture the essential physics of the system. Due to the close agreement with the micromagnetic model, we will use the SA2 model to examine the effects of nonuniform stress on the wall motion.

For all the $s = 300$ nm models, the final resting position of the wall is around 165 nm from the center of contact 2 ($x = -165$ nm). As the initial position of the wall was 165 nm from the center of contact 1 ($x = -465$ nm), the final position relative to contact 2 is exactly the same as the initial position relative to contact 1. Therefore, initializing the wall at $x = -465$ nm ensures that the model describes motion that could be sustained, using additional contacts to propagate the wall down the wire in identical steps of distance equal to s.[18] Similarly, motion in models with $s = 400$ and 500 nm occurred in steps of s when the initial wall position was respectively 215 nm ($x = -615$ nm) and 265 nm ($x = -765$ nm) from the center of contact 1.

An increase in V_C from 0.25 to 1 V progressively increases the electric field and stress gradient (Fig. 2) between the contacts on the piezoelectric, enhancing the amplitude and the frequency of the oscillations in wall velocity [Fig. 5(a)]. At each V_C, motion is composed of an initial phase, where the wall moves a significant distance from the starting point to the first turning point, and an oscillatory phase, during which the wall settles to the energy minimum position [Fig. 5(b)]. As V_C increases, the walls travel further during the initial motion, while the time in the initial phase, t_i, decreases. The oscillatory phase follows the equation of a damped oscillator. The time for the oscillations to decay by a factor of e^{-1}, τ, is determined by the anisotropy of the system, in this case dominated by shape rather than magnetostriction:

$$\tau = \frac{2(1+\alpha^2)}{\alpha\gamma_0 M_S(N_z - N_y)}. \tag{9}$$

Figure 5(b) shows that while the frequency of the oscillations increases with V_C, the envelope of the exponential decay is similar for all V_C, consistent with Eq. (9). However, as the initial amplitude of the oscillations, defined by the stopping position of the initial motion, increases with higher V_C, the time to damp the position oscillations to within ± 5 nm, t_d, increases proportionally. Due to the competing effect of V_C on t_i and t_d, the total time of wall motion, $t_{\mathrm{step}} = t_i + t_d$, is similar for $V_C = 0.25$, 0.5, and 1 V (3.43, 3.19, and 3.48 ns, respectively). To compare the motion of walls moving under different conditions, we use the propagation distance (s) and t_{step} to define the average velocity, $\langle v \rangle$, of the stepwise motion. $\langle v \rangle$ is approximately constant at ~90 m/s for most voltages applied [Fig. 5(c)]. A reduced average velocity is seen only for the smallest V_C (=0.05 V), where the initial motion was so slow that the wall had not even reached the minimum energy position by the time oscillations at higher V_C had damped down. On the other hand, decreasing the electric field by increasing s results in slower initial motion, but the ringing-down time remains constant at around 2 ns (Fig. 6). The overall dependence of the average velocity on s is nonlinear, with $\langle v \rangle$ increasing slightly from 94 to 103 m/s between $s = 300$ and 400 nm, but then decreasing to 71 m/s at $s = 500$ nm [Fig. 5(d)]. Different wall velocities occur when $V_C = 0.5$ V, $s = 500$ nm and $V_C = 0.25$ V, $s = 300$ nm, even though the magnitude of the electric field is the same in each case,[27] highlighting the effect of the electric field distribution on the stress generated at the nanowire.

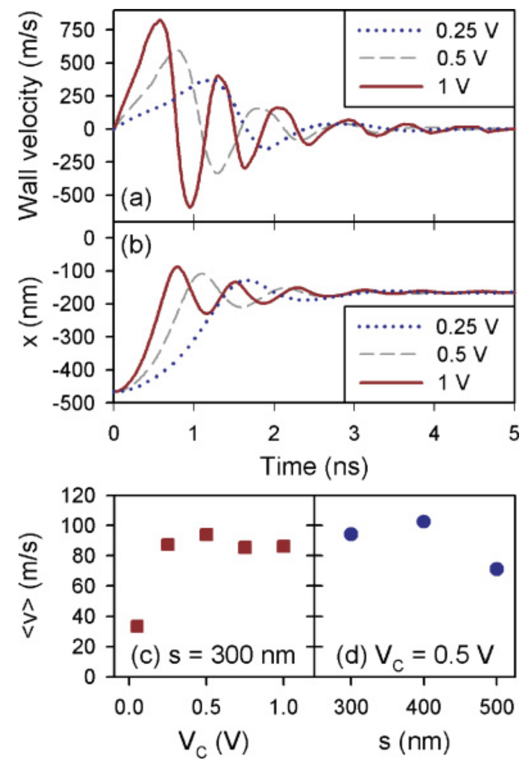

FIG. 5. (Color online) The temporal evolution of (a) the wall velocity and (b) the wall position calculated using SA2 for $V_C = 0.25$, 0.5, and 1 V when $s = 300$ nm. Also shown is the effect of (c) V_C and (d) s on the average velocity $\langle v \rangle$ for stepwise motion over a distance equal to the contact spacing.

In conclusion, a semianalytical model was derived to describe the motion of a domain wall in a magnetostrictive wire under a nonuniform stress. Stress-induced motion is driven by the stress gradient along the direction of propagation. The model is valid for a general stress profile in which the change in stress across the wall width is approximately linear, under the condition that the stress-induced anisotropy never overcomes the shape anisotropy of the wire. For comparisons with previous micromagnetic modeling,[18] we calculated the stress generated by a piezoelectric material contacted by three

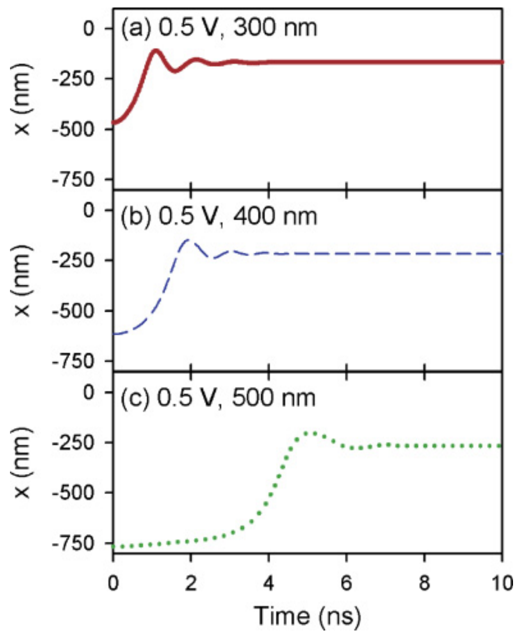

FIG. 6. (Color online) The change in wall position over time under $V_C = 0.5$ V when $s =$ (a) 300, (b) 400, and (c) 500 nm. The initial position of each wall was chosen so that the wall moves a total distance s during the stepwise motion.

electrodes, spaced a distance s along the wire length, with the outer electrodes held at ground and the center electrode at potential V_C. The semianalytical and micromagnetic models were in good agreement, showing that walls can be moved in steps of s along the wire. Characteristically, the steps consist of an initial wall motion toward the central electrode, followed by damped oscillations about the energy minimum position until the wall is stationary. Both the magnitude and spatial distribution of the electric field applied to the piezoelectric, controlled by V_C and s, affect the velocity during the stepwise motion. However, the average velocity of the step is limited to around 100 m/s, due to interplay between the wall velocity during the initial phase of motion and the ringing-down time. As the wall velocity is determined primarily by the axial stress gradient, faster wall velocities could be achieved by tailoring the stress profile to enhance the gradient during the initial motion, but ensure that the wall encounters smaller gradients during the oscillatory phase. Alternatively, it may be possible to change V_C while the wall is still in motion, dynamically switching the stress profile to suppress ringing, enhance the wall velocity, and extend the distance traveled.

APPENDIX A: THE GENERAL SOLUTION TO THE LANDAU-LIFSHITZ-GILBERT EQUATION

Following Slonczewski,[26] the Landau-Lifshitz-Gilbert equation may be written

$$\dot{\vec{m}} = -\frac{\gamma_0}{\mu_0 M_S}\vec{T} + \alpha(\vec{m} \times \dot{\vec{m}}), \tag{A1}$$

where m is the normalized magnetization and T is the torque due to the effective field. In spherical polar coordinates, Eq. (A1) becomes

$$\dot{\theta} = -\frac{\gamma_0}{\mu_0 M_S}\frac{1}{\sin\theta}\frac{\delta W}{\delta\varphi} - \alpha\sin\theta\dot{\varphi}, \tag{A2}$$

$$\sin\theta\dot{\varphi} = \frac{\gamma_0}{\mu_0 M_S}\frac{\delta W}{\delta\theta} + \alpha\dot{\theta}, \tag{A3}$$

where W is the total energy density. The functional derivatives operate as

$$\frac{\delta}{\delta\theta} = \frac{\partial}{\partial\theta} - \nabla\cdot\frac{\partial}{\partial(\nabla\theta)}.$$

From the equations of the domain wall structure we have

$$\dot{\theta} = -\frac{\sin\theta}{\Delta}\dot{q}, \tag{A4}$$

$$\frac{d\theta}{dx} = \frac{\sin\theta}{\Delta}. \tag{A5}$$

Substituting Eq. (A4) into Eqs. (A2) and (A3) and integrating over the domain wall with respect to θ,we obtain

$$-2\frac{\dot{q}}{\Delta} = \int_0^\pi -\frac{\gamma_0}{\mu_0 M_S}\frac{1}{\sin\theta}\frac{\delta W}{\delta\varphi}d\theta - 2\alpha\dot{\varphi},$$

$$2\dot{\varphi} = \int_0^\pi \frac{\gamma_0}{\mu_0 M_S}\frac{\delta W}{\delta\theta}d\theta - 2\alpha\frac{\dot{q}}{\Delta}.$$

Rearrangement of these simultaneous equations gives

$$\dot{\varphi} = \frac{1}{2(1+\alpha^2)}\left(\int_0^\pi \frac{\gamma_0}{\mu_0 M_S}\frac{\delta W}{\delta\theta}d\theta - \alpha\int_0^\pi \frac{\gamma_0}{\mu_0 M_S}\frac{1}{\sin\theta}\frac{\delta W}{\delta\varphi}d\theta\right), \tag{A6}$$

$$\dot{q} = \frac{\Delta}{2\alpha}\left[\int_0^\pi \frac{\gamma_0}{\mu_0 M_S}\frac{\delta W}{\delta\theta}d\theta - 2\dot{\varphi}\right]. \tag{A7}$$

W is the summation of the exchange, demagnetization, Zeeman, and W_k energy densities. The exchange, demagnetization, and Zeeman energy densities can be evaluated in Eqs. (A6) and (A7) to derive the standard 1D model of domain wall motion with an additional contribution from W_k that keeps the solution general:

$$\dot{\varphi} = \frac{1}{2(1+\alpha^2)}\left(2\gamma_0 H_x + \alpha\gamma_0 M_S(N_z - N_y)\sin 2\varphi - \alpha\int_0^\pi \frac{\gamma_0}{\mu_0 M_S}\frac{1}{\sin\theta}\frac{\delta W_k}{\delta\varphi}d\theta + \int_0^\pi \frac{\gamma_0}{\mu_0 M_S}\frac{\delta W_k}{\delta\theta}d\theta\right), \tag{A8}$$

$$\dot{q} = \frac{\Delta}{2\alpha}\left[2\gamma_0 H_x + \int_0^\pi \frac{\gamma_0}{\mu_0 M_S}\frac{\delta W_k}{\delta\theta}d\theta - 2\dot{\varphi}\right]. \tag{A9}$$

Since we wish to solve for a position-dependent W_k, it is necessary to use Eq. (A5) to change the integration variables to x. For a head-to-head wall, the wall boundary is defined by

$$\begin{aligned} \theta &= 0, \quad x = q - \pi\Delta/2, \\ \theta &= \pi, \quad x = q + \pi\Delta/2, \end{aligned} \tag{A10}$$

where q is the position of the wall center and $\pi\Delta$ is the width of the domain wall. Using Eq. (A10), Eqs. (A8) and (A9) become Eqs. (1)–(4) in the main text.

APPENDIX B: DEDUCING f AND g FOR W_k GIVEN BY EQ. (5)

For brevity, Eq. (5) may be rewritten

$$W_k = -\frac{3}{2}\lambda_s\sigma_{xx} + \frac{\mu_0 M_S}{\gamma_0}a\sin^2\theta - \frac{\mu_0 M_S}{\gamma_0}b\sin 2\theta, \qquad \text{(B1)}$$

where

$$a = \frac{3}{2}\frac{\lambda_s\gamma_0}{\mu_0 M_S}(\sigma_{xx} - \sigma_{yy}\sin^2\varphi - \sigma_{zz}\cos^2\varphi - \sigma_{yz}\sin 2\varphi), \qquad \text{(B2)}$$

$$b = \frac{3}{2}\frac{\lambda_s\gamma_0}{\mu_0 M_S}(\sigma_{xy}\sin\varphi + \sigma_{xz}\cos\varphi). \qquad \text{(B3)}$$

Note that a and b are x dependent, since $\sigma_{ij} = \tilde{\sigma}_{ij} + \tilde{\sigma}'_{ij}(x - q)$. As $d\varphi/dx = 0$, we also have

$$a' = \frac{da}{dx} = \frac{3}{2}\frac{\gamma_0}{\mu_0 M_S}(\tilde{\sigma}'_{xx} - \tilde{\sigma}'_{yy}\sin^2\varphi - \tilde{\sigma}'_{zz}\cos^2\varphi - \tilde{\sigma}'_{yz}\sin 2\varphi), \qquad \text{(B4)}$$

$$b' = \frac{db}{dx} = \frac{3}{2}\frac{\gamma_0}{\mu_0 M_S}(\tilde{\sigma}'_{xy}\sin\varphi + \tilde{\sigma}'_{xz}\cos\varphi), \qquad \text{(B5)}$$

$$\frac{d}{dx}\left(\frac{\partial a}{\partial\varphi}\right) = \frac{da'}{d\varphi}, \quad \frac{d}{dx}\left(\frac{\partial b}{\partial\varphi}\right) = \frac{db'}{d\varphi}, \qquad \text{(B6)}$$

which are independent of x and θ. It is also useful to note that by the chain rule

$$\frac{\partial\sigma_{ij}}{\partial\theta} = \tilde{\sigma}'_{ij}\frac{dx}{d\theta}, \quad \frac{\partial a}{\partial\theta} = a'\frac{dx}{d\theta} = a'\frac{\Delta}{\sin\theta}, \quad \text{and} \quad \frac{\partial b}{\partial\theta} = b'\frac{dx}{d\theta} = b'\frac{\Delta}{\sin\theta}. \qquad \text{(B7)}$$

To find f, we substitute Eq. (B1) into Eq. (3) and integrate by parts, making use of the relations in Eq. (B6):

$$\begin{aligned} f &= \int_{q-\pi\Delta/2}^{q+\pi\Delta/2} -\frac{\partial a}{\partial\varphi}\frac{\sin^2\theta}{\Delta} + \frac{\partial b}{\partial\varphi}\frac{\sin 2\theta}{\Delta}dx \\ &= \left[-\frac{\partial a}{\partial\varphi}\left(\int\frac{\sin^2\theta}{\Delta}dx\right) + \frac{\partial b}{\partial\varphi}\left(\int\frac{\sin 2\theta}{\Delta}dx\right)\right]_{q-\pi\Delta/2}^{q+\pi\Delta/2} \\ &\quad - \int_{q-\pi\Delta/2}^{q+\pi\Delta/2} -\frac{\partial a'}{\partial\varphi}\left(\int\frac{\sin^2\theta}{\Delta}dx\right) + \frac{\partial b'}{\partial\varphi}\left(\int\frac{\sin 2\theta}{\Delta}dx\right)dx. \end{aligned}$$

Using Eq. (A5), the remaining integrals can be evaluated by a change of variables:

$$\begin{aligned} f &= \left[-\frac{\partial a}{\partial\varphi}\left(\int\sin\theta d\theta\right) + \frac{\partial b}{\partial\varphi}\left(\int 2\cos\theta d\theta\right)\right]_{q-\pi\Delta/2}^{q+\pi\Delta/2} \\ &\quad - \int_0^\pi -\frac{\partial a'}{\partial\varphi}\left(\int\sin\theta d\theta\right)\frac{\Delta}{\sin\theta} \\ &\quad + \frac{\partial b'}{\partial\varphi}\left(\int 2\cos\theta d\theta\right)\frac{\Delta}{\sin\theta}d\theta \\ &= \left[\frac{\partial a}{\partial\varphi}\cos\theta + 2\frac{\partial b}{\partial\varphi}\sin\theta\right]_{q-\pi\Delta/2}^{q+\pi\Delta/2} - \left[2\Delta\frac{\partial b'}{\partial\varphi}\theta\right]_0^\pi. \end{aligned}$$

Using Eq. (A10) to evaluate the trigonometric terms and substituting in Eq. (B2), this gives Eq. (6) of the main text. To find g, we substitute Eq. (B1) into Eq. (4). Using the relations in Eqs. (A5) and (B7) we have

$$\begin{aligned} g = \int_{q-\pi\Delta/2}^{q+\pi\Delta/2} & -\frac{3}{2}\frac{\lambda_s\gamma_0}{\mu_0 M_S}\tilde{\sigma}'_{xx} + a'\sin^2\theta - b'\sin 2\theta \\ & + \left(a\frac{\sin\theta}{\Delta}\sin 2\theta - 2b\frac{\sin\theta}{\Delta}\cos 2\theta\right)dx. \end{aligned} \qquad \text{(B8)}$$

The term in parentheses in Eq. (B8) contains a mixture of x- and θ-dependent variables, so must be integrated by parts:

$$\begin{aligned} &\int_{q-\pi\Delta/2}^{q+\pi\Delta/2} a\frac{\sin\theta}{\Delta}\sin 2\theta - 2b\frac{\sin\theta}{\Delta}\cos 2\theta dx \\ &= \left[a\left(\int\frac{\sin\theta}{\Delta}\sin 2\theta dx\right) - 2b\left(\int\frac{\sin\theta}{\Delta}\cos 2\theta dx\right)\right]_{q-\pi\Delta/2}^{q+\pi\Delta/2} - \int_{q-\pi\Delta/2}^{q+\pi\Delta/2} a'\left(\int\frac{\sin\theta}{\Delta}\sin 2\theta dx\right) - 2b'\left(\int\frac{\sin\theta}{\Delta}\cos 2\theta dx\right)dx, \\ &= \left[a\left(\int\sin 2\theta d\theta\right) - 2b\left(\int\cos 2\theta d\theta\right)\right]_{q-\pi\Delta/2}^{q+\pi\Delta/2} - \int_{q-\pi\Delta/2}^{q+\pi\Delta/2} a'\left(\int\sin 2\theta d\theta\right) - 2b'\left(\int\cos 2\theta d\theta\right)dx \\ &= \left[a\left(\sin^2\theta - \frac{1}{2}\right) - b\sin 2\theta\right]_{q-\pi\Delta/2}^{q+\pi\Delta/2} - \int_{q-\pi\Delta/2}^{q+\pi\Delta/2} a'\left(\sin^2\theta - \frac{1}{2}\right) - 2b'\sin 2\theta\, dx \end{aligned} \qquad \text{(B9)}$$

where the integrals in parentheses have been solved using a change of variables. Inserting Eq. (B9) into Eq. (B8) and evaluating the remaining integrals gives

$$g = \left[-\frac{3}{2}\frac{\lambda_s\gamma_0}{\mu_0 M_S}\tilde{\sigma}'_{xx}x + a\left(\sin^2\theta - \frac{1}{2}\right) - b\sin 2\theta + \frac{a'}{2}x\right]_{q-\pi\Delta/2}^{q+\pi\Delta/2}.$$

Hence using Eq. (A10), we find Eq. (7) of the main text.

APPENDIX C: THE DOMAIN WALL WIDTH PARAMETER

The magnetostriction energy is defined by Eq. (5) in the main text, and the exchange and demagnetization energies by

$$W_{ex} = A(\nabla\theta)^2, \tag{C1}$$

$$W_d = \frac{\mu_0 M_S^2}{2}\left(N_y\alpha_y^2 + N_z\alpha_z^2\right), \tag{C2}$$

where $\alpha_x = \cos\theta, \alpha_y = \sin\theta\sin\varphi$, and $\alpha_z = \sin\theta\cos\varphi$. Minimization of the energy density with respect to θ gives

$$\frac{\delta(W_d + W_{ex} + W_k)}{\delta\theta} = 0 = \frac{\partial}{\partial\theta}(W_d + W_k) - \nabla\cdot\frac{\partial W_{ex}}{\partial(\nabla\theta)},$$

$$\frac{\delta(W_d + W_{ex} + W_k)}{\delta\theta} = \frac{\partial}{\partial\theta}(W_d + W_k) - 2A\nabla^2\theta = 0. \tag{C3}$$

Using the identity $\frac{d}{dx}[(\nabla\theta)^2] = 2\frac{d\theta}{dx}\nabla^2\theta$, Eq. (C3) can be multiplied by $d\theta/dx$ and integrated with respect to x to give

$$W_d + W_k - A\left(\frac{d\theta}{dx}\right)^2 = 0. \tag{C4}$$

Substituting in Eqs. (A5), (C2), and (5), evaluating at the wall center ($x = q, \theta = \pi/2$), and rearranging gives Eq. (8) in the main text.

[1] D. Atkinson, D. A. Allwood, G. Xiong, M. D. Cooke, C. C. Faulkner, and R. P. Cowburn, Nat. Mater. **2**, 85 (2003).
[2] M. Hayashi, L. Thomas, C. Rettner, R. Moriya, Y. B. Bazaliy, and S. S. P. Parkin, Phys. Rev. Lett. **98**, 037204 (2007).
[3] G. S. D. Beach, C. Knutson, C. Nistor, M. Tsoi, and J. L. Erskine, Phys. Rev. Lett. **97**, 057203 (2006).
[4] M. Hayashi, L. Thomas, Y. B. Bazaliy, C. Rettner, R. Moriya, X. Jiang, and S. S. P. Parkin, Phys. Rev. Lett. **96**, 197207 (2006).
[5] A. Thiaville, J. M. Garcia, and J. Miltat, J. Magn. Magn. Mater. **242**, 1061 (2002).
[6] Y. Nakatani, A. Thiaville, and J. Miltat, Nat. Mater. **2**, 521 (2003).
[7] D. G. Porter and M. J. Donahue, J. Appl. Phys. **95**, 6729 (2004).
[8] M. T. Bryan, T. Schrefl, and D. A. Allwood, IEEE Trans. Magn. **46**, 1135 (2010).
[9] J. S. Dean, M. T. Bryan, D. A. Allwood, S. Bance, M. A. Bashir, G. Hrkac, A. Goncharov, and T. Schrefl, IEEE Trans. Magn. **45**, 4067 (2009).
[10] J. M. Blanco, V. Zhukova, M. Ipatov, and A. Zhukov, Phys. Status Solidi A **208**, 545 (2011).
[11] M. T. Bryan, S. Bance, J. Dean, T. Schrefl, and D. A. Allwood, J. Phys.: Condens. Matter. **24**, 024205 (2012).
[12] M. T. Bryan, T. Schrefl, D. Atkinson, and D. A. Allwood, J. Appl. Phys **103**, 073906 (2008).
[13] A. Kunz and S. C. Reiff, J. Appl. Phys. **103**, 07D903 (2008).
[14] A. Kunz and S. C. Reiff, Appl. Phys. Lett. **93**, 082503 (2008).
[15] C. Y. You, Appl. Phys. Lett. **92**, 192514 (2008).
[16] C. Y. You, Appl. Phys. Lett. **92**, 152507 (2008).
[17] T. K. Chung, G. P. Carman, and K. P. Mohanchandra, Appl. Phys. Lett. **92**, 112509 (2008).
[18] J. Dean, M. T. Bryan, T. Schrefl, and D. A. Allwood, J. Appl. Phys. **109**, 023915 (2011).
[19] J. T. Heron, M. Trassin, K. Ashraf, M. Gajek, Q. He, S. Y. Yang, D. E. Nikonov, Y. H. Chu, S. Salahuddin, and R. Ramesh, Phys. Rev. Lett. **107**, 217202 (2011).
[20] A. E. Clark, J. B. Restorff, M. Wun-Fogle, T. A. Lograsso, and D. L. Schlagel, IEEE Trans. Magn. **36**, 3238 (2000).
[21] A. E. Clark, M. Wun-Fogle, J. B. Restorff, T. A. Lograsso, and J. R. Cullen, IEEE Trans. Magn. **37**, 2678 (2001).
[22] M. W. Hooker, NASA Report No. NASA/CR-1998-208708, 1998, (unpublished).
[23] Computer program COMSOL MULTIPHYSICS, [www.comsol.com].
[24] J. Dean, M. T. Bryan, G. Hrkac, A. Goncharov, C. L. Freeman, M. A. Bashir, T. Schrefl, and D. A. Allwood, J. Appl. Phys. **108**, 073903 (2010).
[25] D. Damjanovic, Rep. Prog. Phys. **61**, 1267 (1998).
[26] J. C. Slonczewski, Int. J. Magn. **2**, 85 (1972).
[27] The gap between the contacts is $s - 100$ due to the contact width, so the electric field is $V_C/(s - 100)$.